Contents lists available at ScienceDirect

Nano Energy
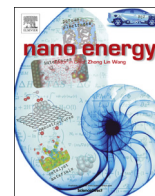
Communication

Chestnut-like SnO$_2$/C nanocomposites with enhanced lithium ion storage properties

CrossMark

Lie Yang [a], Tao Dai [a], Yuecun Wang [a], Degang Xie [a], R. Lakshmi Narayan [a,b], Ju Li [a,c,*], Xiaohui Ning [a,**]

[a] Center for Advancing Materials Performance from the Nanoscale (CAMP-Nano), State Key Laboratory for Mechanical Behavior of Materials, Xi'an Jiaotong University, Xi'an 710049, PR China
[b] Department of Materials Science and Engineering, Carnegie Mellon University, Pittsburgh, Pennsylvania 15213, USA
[c] Department of Nuclear Science and Engineering, and Department of Materials Science and Engineering, Massachusetts Institute of Technology, Cambridge, Massachusetts 02139, USA

ABSTRACT

Chestnut-like SnO$_2$ and SnO$_2$/C nanocomposites with hierarchical structures are synthesized by hydrothermally oxidizing Sn nanoparticles in glucose solution. Structural characterizations using SEM and TEM reveal that the SnO$_2$ nanoparticles are composed of numerous, randomly arranged SnO$_2$ nanosheets with hollow cores. Owing to the short electron and ion diffusion distances and transformation strain accommodation mechanism of this structure the new SnO$_2$/C nanocomposites exhibit enhanced lithium ion storage properties with a capacity of $\sim$930 mAh g^{-1} and capacity retention of about 96% after 100 cycles at 0.1 C. An *in situ* TEM study of the electrochemically driven lithiation/delithiation of SnO$_2$/C nanocomposites reveals that their enhanced cycling stability is mainly facilitated by the limited volume expansion and excellent mechanical robustness of the hollow chestnuts.

© 2016 Elsevier Ltd. All rights reserved.

1. Introduction

With the rapid development of portable electronic devices, electric vehicles and stationary power storage, lithium ion batteries (LIBs) are now required to have a higher energy density and longer cycle life [1,2]. In that context, SnO$_2$ has been identified as a promising anode material and has garnered a lot of attention, prompting many studies on its application prospects. However, while SnO$_2$ possesses a theoretical capacity of 782 mAh g^{-1} [3,4], a value which is nearly twice that of commercially used graphite, it undergoes severe capacity fade during charge/discharge cycles [5,6], thereby hindering its practical application.

The underlying cause for capacity fade, as revealed by transmission electron microscope (TEM) observations [7,8] and X-ray tomography [9] studies is that, SnO$_2$ undergoes a large volume expansion/contraction cycle during the lithiation/delithiation process, leading to its fracture and pulverization. Post fracture, the freshly formed SnO$_2$ surfaces continuously participate in side reactions with the electrolyte and get covered with an insulating

solid electrolyte interphase (SEI) [10]. This manifests as a loss of electrical contact between the pulverized SnO$_2$ particles and the current connecter, thus triggering capacity fade. To solve this problem, various types of nanosized SnO$_2$ composites such as nanoparticles [11], nanosheets [12–15], nanowires [16], nanotubes [17], hollow particles [18], porous particles [19], core shell particles [20], yolk shell particles [21] and hierarchical hollow particles [3,22,23], have been synthesized. Owing to their clever structural design and nanoscale dimensions, these composites exhibit enhanced cycling stability. In particular, the use of hierarchical hollow SnO$_2$/C nanoparticles is enticing because of shorter electron and ion diffusional hopping distances and buffer volumes to accommodate transformation strains. However, since they are synthesized on hard templates, like silica [24] or polystyrene (PS) [3,22] particles, an additional post-processing step for the removal of these templates is essential, which increases the cost. Moreover, during synthesis, a high degree of precision and control needs to be exercised while fixing the pH values of the reactants [12,22]. Hence, these multiple complexities restrict the mass production of hierarchical hollow SnO$_2$/C to some extent.

To alleviate these production issues, we developed a facile hydrothermal method to prepare hierarchical hollow SnO$_2$/C particles with a structure similar to that of the shell of a chestnut. The as-synthesized chestnut-like SnO$_2$/C particles exhibit improved lithium storage properties and capacity retention when used as an

---

* Corresponding author at: Center for Advancing Materials Performance from the Nanoscale (CAMP-Nano), State Key Laboratory for Mechanical Behavior of Materials, Xi'an Jiaotong University, Xi'an 710049, PR China.
** Corresponding author.
E-mail addresses: liju@mit.edu (J. Li), xiaohuining@mail.xjtu.edu.cn (X. Ning).

anode for lithium ion batteries. We study the growth mechanism of these particles by extracting the reaction products at specific intervals and observing them under the scanning electron microscope (SEM) and transmission electron microscope (TEM). Finally, we conduct real-time lithiation/delithiation experiments on the particles inside a TEM and observe morphological changes that explain their enhanced performance as a battery material.

2. Experimental section

2.1. Sample preparation

The schematic in Fig. 1a shows the preparation process for chestnut-like SnO_2/C nanocomposites. First, Sn nanoparticles (NPs) were prepared by reducing $SnCl_2$ with $NaBH_4$ [25]. For this, 0.40g polyvinyl pyrrolidone (PVP, K30, AR, Aladdin) was dissolved in 90 mL diethylene glycol (DEG, AR, Aladdin) by magnetic stirring and ultrasound agitation. This solution was then heated up to 90 °C in an oil bath following which, 0.95 g $SnCl_2$ (AR, Aladdin) was added to it under magnetic stirring. After the $SnCl_2$ salts completely dissolved, 0.87 g $NaBH_4$ (AR, Aladdin), dissolved in 8.0 mL DEG, was added into the solution drop wise in the span of 10 min with accompanied stirring. The solution was subsequently cooled to ambient temperature, centrifuged at 9000 r min^{-1}, washed with ethanol and water and air-dried at 80 °C for several hours.

The following describes how these as-prepared Sn nanoparticles were hydrothermally treated in glucose solution to obtain chestnut-like SnO_2 nanoparticles. First, 0.10g as-prepared Sn NPs and 0.10g glucose (AR, Aladdin) were dispersed and dissolved into 20 mL distilled water by ultrasound agitation for 30 min. Then, the suspension was transferred into a 100 mL Teflon-lined stainless steel autoclave and kept in an electric oven at 180 °C for 20 h. Light yellow products were collected by centrifugation, water washing, and air drying at 80 °C. Finally, SnO_2 nanoparticles were obtained by further heating the light yellow products at 400 °C for 2 h in air with a heating rate of 1 °C min^{-1}.

To impart a carbon coating to these particles, a uniform mixture of oleic acid (AR, Aladdin) and as-prepared SnO_2 particles with mass ratio of 2.5:1 was calcined at 400 °C under Ar for 2 h at a ramping rate of 1 °C min^{-1}.

2.2. Morphological and structural characterization

The morphologies of samples were characterized with a field emission scanning electron microscope (SEM, Hitachi SU6600). The inner structure and chemical composition of the samples was investigated with a transmission electron microscope (TEM, JEOL 2100 F, accelerating voltage of 200 kV), which is equipped with energy-dispersive X-ray spectroscopy (EDS). X-ray diffraction (XRD) measurements were carried out with a Bruker D8 Advance diffractometer to study the crystalline structure of the samples.

2.3. Electrochemical measurements

To assess the lithium ion storage capability of as-prepared SnO_2/C, it was assembled as a working electrode of CR2032 coin cells. The SnO_2/C electrode was prepared by mixing chestnut-like SnO_2/C particles (80 wt%) with 10 wt% conductive carbon black (Super-P) and 10 wt% poly(vinylidene fluoride) (PVDF, AR, Aladdin) binder in N-methyl-2-pyrrolidone (NMP, AR, Aladdin) solvent. Subsequently, the obtained slurry was coated on copper foil and dried at 80 °C for 24 h. The mass loading was controlled to $\sim$0.5 mg cm^{-2}. Pure lithium foils were used as both the working and reference electrode. The electrolyte was 1.0 M $LiPF_6$ dissolved in a mixture of ethylene carbonate (EC) and diethyl carbonate (DEC) with a volume ratio of EC/DEC=1:1. This cell was assembled in an Ar-filled glove box (Unilab, MBraun) where the concentrations of moisture and oxygen were maintained below 0.1 ppm. Galvanostatic charge-discharge performance tests were carried out with a battery tester (BST8-MA, MTI) at various current densities between 0.005 and 2.50 V. Cyclic voltammetry (CV) measurements were performed at a scanning rate of 0.5 mV s^{-1} within a potential window of 0–2.5 V on a CHI 660E electrochemical workstation (Shanghai Chenhua). It should be noted that the total weight of SnO_2 and the carbon layer (SnO_2/C) was used to calculate the specific capacity values.

2.4. In situ TEM observation

The *in situ* TEM characterization was carried out in an environmental transmission electron microscope (ETEM, Hitachi H9500, 300 kV) using the PI 95 H1H holder (Hysitron). An all-solid nanobattery was assembled. The cluster of chestnut-like SnO_2/C nanocomposites attached to an aluminum plate with conductive silver epoxy was set as the working electrode, and Li metal loaded on a tungsten tip was set as the counter electrode. 2 Pa CO_2 was
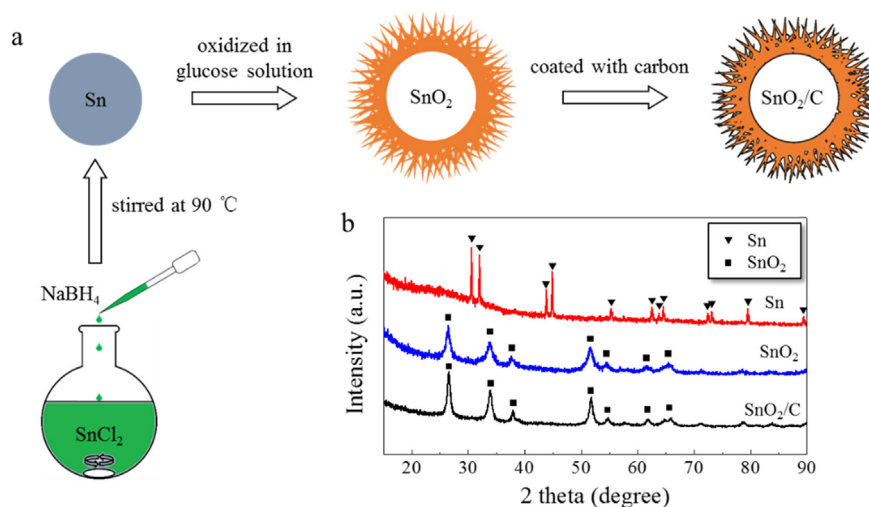

Fig. 1. (a) Schematic illustration of the preparation process for chestnut-like SnO_2/C nanocomposites; (b) corresponding XRD patterns of the products obtained at each step.

pumped into the ETEM chamber which reacted with the naturally formed Li_2O surface layer on Li metal to form Li_2CO_3. Li_2CO_3 served as the solid electrolyte and was much more stable under electron beam irradiation than the widely used Li_2O [26]. A bias potential of −4.0 V was applied to the chestnut-like SnO_2/C nanocomposites to initiate the lithiation, while the bias was reversed to facilitate delithiation. More than 10 fully reversed cycles of bias potential were employed to test the cycling stability of these particles.

3. Results and discussions

Sn nanoparticles, the precursors in the synthesis of SnO_2/C nanocomposites, are fully dense spheres with an average diameter of about 110 nm (See Fig. S1a–b in Supplementary information (SI)). The XRD results shown in Fig. 1b (red curve), confirm that they exist in the form of pure crystalline tetragonal white tin. After these Sn particles are oxidized in glucose solution during the hydrothermal treatment, hierarchical hollow nanoparticles are produced (See Fig. S1c–d). XRD patterns in Fig. 1b (blue curve) reveal that the oxidized nanoparticles are tetragonal rutile SnO_2. The shell of an individual SnO_2 nanoparticle is composed of many randomly arranged nanosheets, as shown in the magnified SEM image in Fig. 2a. Since the structural morphology of these particles is similar to that of a 'chestnut', shown as a reference in Fig. 2b, these SnO_2 nanoparticles will hereafter be referred to as 'chestnut-like nanoparticles'. These unique structures contain multiple layers of SnO_2 nanosheets and vast inner void spaces which bestow them with high specific surface area and large buffer volume. A conductive carbon layer is coated on the surface of these chestnut-like nanoparticles to improve their electrical conductivity. A high resolution TEM (HRTEM) image of the edge of a chestnut-like SnO_2/C particle in Fig. 2c shows that a compact amorphous carbon layer, measuring 5–10 nm in thickness, is formed. In addition to imparting a high quality carbon coat, the chestnut-like structure of the obtained SnO_2/C particle remains unaffected (see Fig. S1e–f of SI) by the coating treatment.

Beneath the carbon layer, SnO_2 exists in the crystalline state as seen from the XRD pattern shown in Fig. 1b (black curve). Also, a lattice spacing of 3.4 Å measured from the inset of Fig. 2c matches well with the (110) plane of rutile SnO_2, thereby suggesting that the preferential growth direction of SnO_2 nanosheets is [110]. The selected area electron diffraction (SAED) pattern shown in Fig. 2d further confirms the polycrystalline nature of the chestnut-like SnO_2/C composites. The energy-dispersive X-ray spectroscopy (EDS) element mapping of the composite nanoparticle in Fig. 2e reveals that the spatial distribution of carbon (Fig. 2h) superimposes perfectly over that of SnO_2 (Fig. 2f–g), thus suggesting an intimate contact between the two materials.

To understand the transformation of chestnut-like SnO_2 nanoparticles from the initial spherical solid Sn nanoparticles, samples are extracted from the reaction mix at different times. In Fig. 3a–h, the SEM and TEM images of the typical products obtained after a reaction time of 0 h, 3 h, 5 h and 20 h, respectively are shown. At 0 h, or as the initial condition before oxidation in glucose solution, the pristine Sn nanoparticle is a spherical solid with a smooth surface as seen in Fig. 3a–b. However, after 3 h the surface gets a rough appearance (see Fig. 3c–d) owing to numerous nano-protrusions appearing around the surface of the nanoparticles. Around the same time, the inner Sn core starts shrinking, such that the solid particle now gets a shell-like structure. When the reaction time progresses to 5 h, the Sn core shrinks further and a few tiny sheets of SnO_2 could be observed on the surface of the particle (refer to Fig. 3e–f). Finally, after 20 h, the core is completely consumed and a chestnut-like hierarchical hollow structure is obtained (see Fig. 3g–h).

Additionally, during the transformation of chestnut-like SnO_2, the phase evolution of these nanoparticles is also simultaneously tracked using XRD. It is observed that as the reaction time increases, the intensity of peaks representing tetragonal white Sn decreases gradually, thus suggesting that the pristine Sn nanoparticles are getting oxidized continuously. This inference is consistent with the observation of shrinkage and consumption of Sn cores seen in Fig. 3c–h. The appearance of characteristic peaks of both SnO and SnO_2 at 3 h and 5 h suggests a possible two-step oxidation of Sn nanoparticles under this hydrothermal condition.
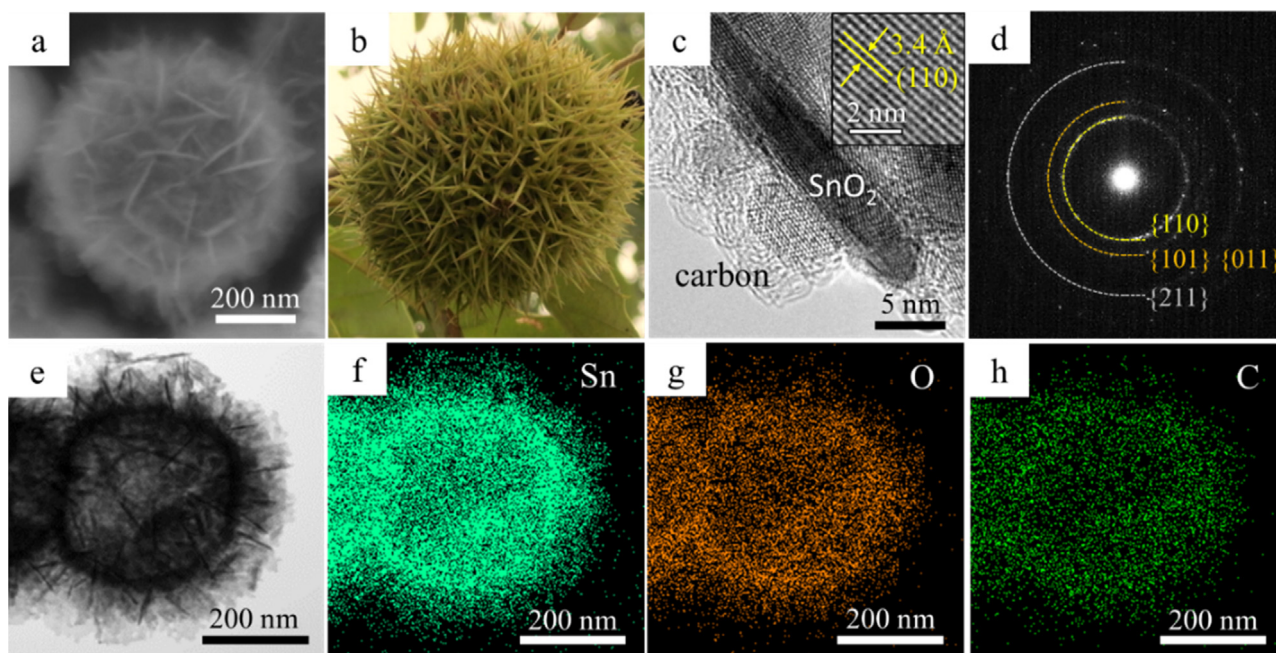
Fig. 2. Morphological and compositional characterizations. (a) SEM image of a single SnO_2 particle; (b) photograph of a chestnut seed (*Castanea*); (c) high resolution TEM (HRTEM) image of the surface of a SnO_2/C particle. The inset shows the lattice image of SnO_2 nanosheet; (d) SAED pattern of a single SnO_2/C particle; (e) bright field (BF) scanning transmission electron microscope (STEM) image of a single SnO_2/C particle; (f–h) Sn, O, and C elements mapping of the SnO_2/C particle shown in (e).
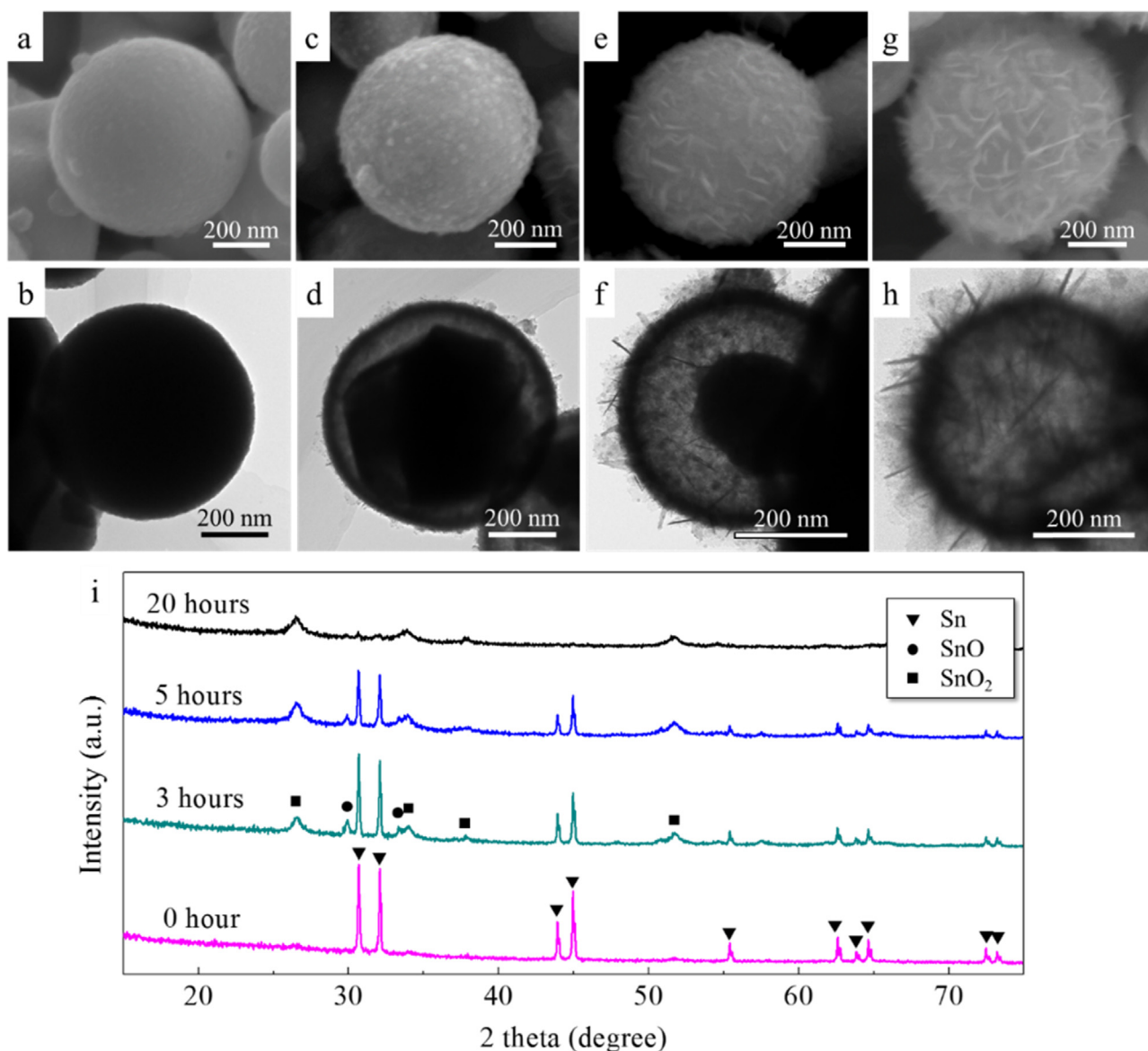
Fig. 3. *Ex situ* SEM and TEM observation of typical SnO_x particles obtained at increasing reaction time: (a–b) 0 h, (c–d) 3 h, (e–f) 5 h, (g–h) 20 h; (i) corresponding XRD patterns of SnO_x particles.

However, after 20 h, XRD only shows characteristic peaks of SnO_2 implying that all the Sn nanoparticles are eventually oxidized to SnO_2.

Based on the above described structural and compositional changes, the transformation of Sn nanoparticles into hollow structures can be explained as the following. In the initial stages, the outer surfaces of Sn nanoparticles are oxidized by reacting with water: $Sn+H_2O=SnO+H_2$. Now, due to the difference in diameters and charge states of the ions, the outward diffusion of Sn ions is much faster than that of oxygen ions diffusing inwards [27]. Therefore, to balance the net effect of outward diffusion, there is a net inward flux of vacancies. These out-of-equilibrium vacancies accumulate into voids that merge into a large void sheath. Such a voiding mechanism was previously observed in ZnO_2 and CoO nanoparticles and is understood as an extreme limit of the Kirkendall effect [17,28,29]. The temperature of the hydrothermal treatment (180 °C) is very close to the melting point of metallic tin (232 °C), so surface/interfacial diffusion of Sn/Sn^{x+} should be operative. The residual Sn core still contacts the oxide at points due to adhesion, providing Sn source for oxide growth.

With time, the Sn cores get fully consumed by the growing voids and eventually result in spherical hollow structures.

To understand how randomly arranged SnO_2 nanosheets form on the outer surface of the SnO_2 particle, we synthesized a batch of particles without adding glucose to the reaction mix. When we compare the final product obtained with and without the addition of glucose (see Fig. S2), it was noted that the former imparts a chestnut-like morphology while the latter preserves the initial spherical shape of the Sn particle. This implies that the presence of glucose plays a crucial role in the formation of the randomly arranged nanosheets. Previous studies have shown that glucose is hydrolyzed into small functional groups under hydrothermal conditions [30,31]. Since such functional groups should also form in our synthesis, we believe that they may get absorbed on some specific lattice planes of SnO_2 and suppress crystal growth along certain directions. Therefore, nanosheets form only along certain preferred directions and from HRTEM images, the plane normal was determined to be the [110] direction.
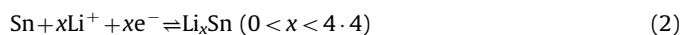
From the preceding discussion it is evident that our method of synthesizing SnO_2 nanoparticles is less complicated and uses
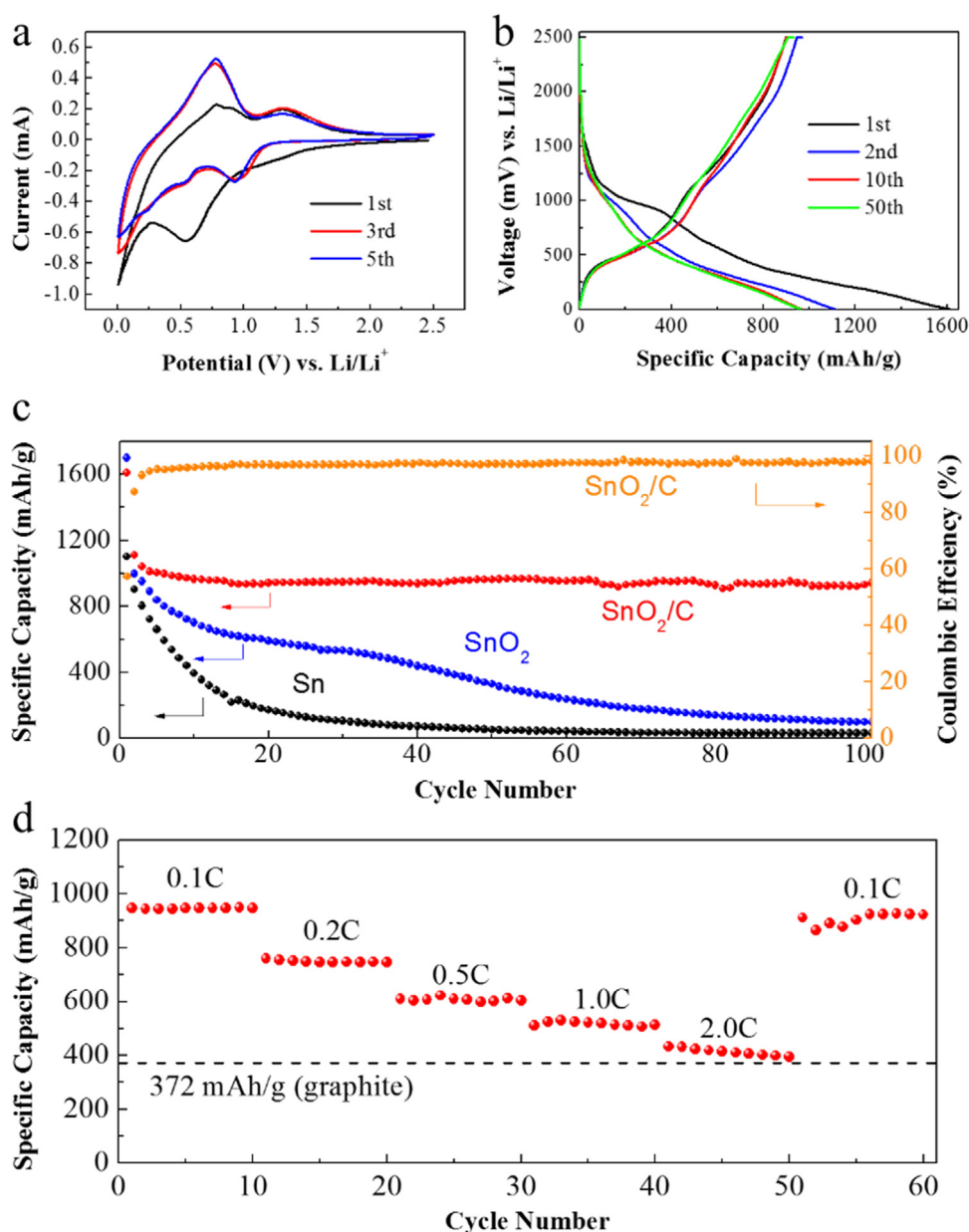
Fig. 4. Electrochemical performance of chestnut-like SnO$_2$/C nanocomposites. (a) Representative cyclic voltammograms (CV) at a scanning rate of 0.5 mV s^{-1}; (b) charge/discharge voltage profiles for the 1st, 2nd, 10th, and 50th cycles at a current density of 0.1 C; (c) cycle performance at a current density of 0.1 C (arrows indicate the reference axes); (d) rate capability of chestnut-like SnO$_2$/C.

lesser number of reactants (see Table S1) compared to other methods that require hard templates and precise pH control [12,15,22,23]. In the following paragraphs, we will look at the advantages of chestnut-like SnO$_2$/C nanocomposites possessing unique structural attributes like high specific surface area, large void space and highly conductive surface coating. These features will be discussed in the context of designing and utilizing chestnut-like SnO$_2$/C nanoparticles as anode materials for LIBs.

Variations of current, mA, and potential, V, obtained from the cyclic voltammetry experiments of the present nanocomposites is displayed in Fig. 4a. In this plot, the strong cathodic peak observed at 0.55 V in the first cycle can be attributed to the reduction of SnO$_2$ to Sn, as described by Eq. (1) [32], and the formation of a solid electrolyte interphase (SEI) layer. And, the current peak at 0.01 V corresponds to an alloying process that forms Li$_x$Sn according to Eq. (2) [32].

$$SnO_2 + 4Li^+ + 4e^- \rightleftharpoons Sn + 2Li_2O \qquad (1)$$

$$Sn + xLi^+ + xe^- \rightleftharpoons Li_xSn \ (0 < x < 4 \cdot 4) \qquad (2)$$

In the anodic process of the first cycle, the peaks at 0.78 V and 1.30 V correspond to the de-alloying of Li$_x$Sn and partial reversible formation of SnO$_2$, respectively, as established by previous studies [33,34]. However, in the 3rd and 5th cycles, nearly no peaks are observed at 0.55 V, indicating that the formation of SEI is mitigated or even terminated. Additionally, it can be seen that the CV curves of the 3rd and 5th cycle overlap with each other, therefore suggesting that the electrochemical reactions are fully reversible.

To assess the cycling stability of these materials during charging and discharging, the voltage profiles as a function of specific capacity, at the current density of 0.1 C are shown in Fig. 4b. Note that the current density of 1.0 C corresponds to 782 mA g^{-1}. While
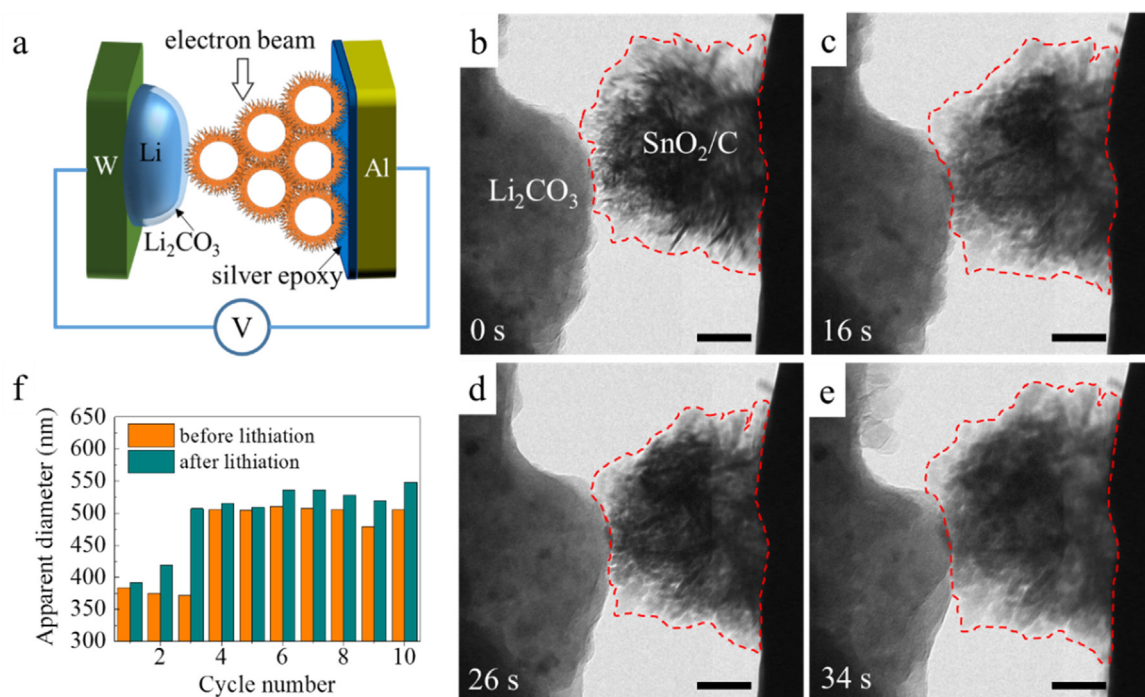
Fig. 5. *In situ* TEM observation of the morphology evolution of chestnut-like SnO$_2$/C nanocomposites during lithiation/delithiation process. (a) schematic illustration for the nanobattery set-up; (b–e) still frames extracted from the recorded movie during 1st and 2nd lithiation/delithiation cycle, (b) pristine cluster, (c) after 1st lithiation, (d) after 1st delithiation, (e) after 2nd lithiation, scale bar: 100 nm; see also Movie S1 to appreciate the accordion-like motion. (f) apparent diameters of SnO$_2$/C clusters during cyclic lithiation/delithiation process.

the initial discharge capacity is found to be as high as 1600 mAh g^{-1}, the subsequent charge capacity decreases to 900 mAh g^{-1}, recording a capacity loss of ~44%. This large capacity loss is mainly caused by the inevitable formation of the SEI layer and incomplete extraction of lithium from the active material. However, in the same figure, it can be seen that the capacity losses are largely reduced subsequent to the second cycle, such that only 0.4% capacity fade was observed between the 10th cycle and 50th cycle, with a capacity loss rate of only ~10^{-4} per cycle, which is extraordinary. Besides, we can see that the curve of the 10th cycle almost overlaps with the curve of the 50th cycle, which again highlights the excellent cycling stability and reversibility of these SnO$_2$/C chestnuts.

To examine the cycling stability further, the specific capacity of SnO$_2$/C is plotted as a function of the number of cycles in Fig. 4c. As can be seen here, SnO$_2$/C exhibits a uniform discharge capacity of 930 mAh g^{-1} even after 100 cycles. Interestingly, this value is higher than the theoretical capacity of SnO$_2$, which is ~782 mAh g^{-1}, provided that the only active chemical reaction occurring is the one shown in Eq. (2). Therefore, our SnO$_2$/C nanocomposites can display additional capacity only if the reaction shown in Eq. (2) and the partial reversal of the redox reaction described in Eq. (1) [3,25,35] occur concurrently. This is confirmed by SAED and XRD characterization of fully charged active particles that exhibit signals of both Sn and SnO$_2$, as shown in Fig. S3. Note that, the capacity retention ratio of SnO$_2$/C is as high as 96% after 100 cycles, which is significantly higher than those reported in the literature for other SnO$_2$ based hierarchical particles (see Table S2). This enhanced cycling stability can be ascribed to the large void space of chestnut-like structure, which buffers the volume expansion of both the single SnO$_2$/C particle and the electrode film, thus maintaining its electron conduction integrity and facilitating the high level utilization of SnO$_2$.

For a more comprehensive evaluation of our SnO$_2$/C nanocomposites, the electrochemical behavior of bare Sn nanoparticles and bare chestnut-like SnO$_2$ are also evaluated by galvanostatic

charge/discharge experiments and the results are included in Fig. 4c. It can be seen that compared to the SnO$_2$/C particle, both chestnut-like SnO$_2$ particles without carbon and bare Sn nanoparticles exhibit faster capacity fading rate as their remaining capacity decreases to about 98 mAh g^{-1} after 100 cycles and 100 mAh g^{-1} after just 30 cycles, respectively. Bare Sn particles display poor cycling stability because their drastic dimensional changes cause SEI instability that disrupts and destroys electron conduction path during cycling. As a result, bare Sn particles are not efficiently utilized if used in the cell reactions. However, as an embedded part of the oxide-metal composite formed after the initial reaction shown in Eq. (1), due to the constraining effect of the surrounding Li$_2$O oxide that suppresses SEI instability somewhat, Eq. (2) can proceed reversibly for the embedded Sn particles. On the other hand, the performance difference between chestnut-like SnO$_2$/C and SnO$_2$ particles can be ascribed to the coated protective carbon layer which separates SnO$_2$ from the electrolyte, preventing the SEI from forming directly on the surface of SnO$_2$, and making electron conduction paths even more difficult to disrupt. This observation suggests that it is necessary to coat carbon on SnO$_2$ particles to facilitate their superior performance.

Additionally, as shown in Fig. 4d, chestnut-like SnO$_2$/C particles exhibit good rate capability with the discharge capacities of 945, 750, 610, 520 and 410 mAh g^{-1} at the current densities of 0.1 C, 0.2 C, 0.5 C, 1 C and 2 C, respectively. Remarkably, when the current density was restored to 0.1 C after 2 C testing, about 97.8% (925 mAh g^{-1}) of the initial specific capacity was retained, revealing robustness of the SnO$_2$/C electrode. It is believed that this good rate capability is associated with the nanostructure which shortens the diffusional hopping distances of lithium ions and electrons within the nanocomposite.

To explain the enhanced stability of the chestnut-like SnO$_2$/C particles, *in situ* TEM measurements were performed to observe the morphological evolution of chestnut-like SnO$_2$/C nanocomposites during the lithiation/delithiation process. A schematic illustration of the all-solid nanobattery is shown in Fig. 5a. By

biasing SnO_2/C nanocomposites with a potential of -4.0 V, lithiation was initiated. As shown in Fig. 5b–e and Movie S1, during the first two cycles, the cluster expanded and contracted reversibly like an accordion, suggesting excellent reversibility. The chestnut-like structure does not develop any cracks, suggesting a high degree of structural integrity during the cyclic lithiation and delithiation. Subsequently, bias potentials of -4.0 V and $+4.0$ V were applied repeatedly for ten cycles. During these cycles, the apparent diameter for a particular combination of lithiation and delithiation cycle is quite stable, as seen in Fig. 5f. It should be noted that the sudden increase in the apparent diameter after lithiation in the 3rd cycle derives little contribution from the lithiation process, but is rather a result of the movement of the aluminum current collector, which exposes a higher proportion of SnO_2/C nanocomposites in the TEM view (see Movie S2). For all individual cycles considered, the calculated increase of apparent diameter after lithiation is consistently less than 12%. This value is much lower than that seen for pure SnO_2 which shows an increase of $\sim 34\%$ [36]. Note that fully dense SnO_2 nanoparticles can only expand laterally during lithiation. On the other hand, since the hollow core and sheet-configuration of the chestnut-like SnO_2/C nanoparticles leaves a large buffering space for volume expansion, the medial and lateral movement of the active materials is facilitated. Therefore, the chestnut-like SnO_2/C nanoparticles undergo smaller apparent volume changes during lithiation/delithiation as seen from the *in situ* TEM movies and images. Owing to such facial accommodation mechanism of the transformation strains, chestnut-like SnO_2/C nanocomposites exhibit a remarkable ability to reversibly undergo cyclic electrochemical changes without fatigue induced failure. In summary, by utilizing the *in situ* TEM technique we demonstrate that the chestnut-like SnO_2/C nanocomposites exhibit excellent structural integrity and reversibility, remarkable toughness and minimal volume expansion during cyclic lithiation and delithiation process. These attributes are critical for maintaining a high utilization ratio of active SnO_2/C materials and promote enhanced cycling stability of chestnut-like SnO_2/C particles as seen from their electrochemical performance.

Supplementary material related to this article can be found online at http://dx.doi.org/10.1016/j.nanoen.2016.08.060.

4. Conclusions

We have developed a facile hydrothermal method to synthesize chestnut-like hierarchical hollow SnO_2 nanoparticle and SnO_2/C nanocomposite. The unique burr structure of the SnO_2 presents shorter electron and ion diffusional hopping distances and buffer volume, such that the SnO_2/C nanocomposite shows good electrochemical performance as the anode of a lithium ion battery. These chestnut-like nanocomposites with size of about 400 nm exhibit high reversible specific capacity of 930 mAh g^{-1} and capacity retention of about 96% after 100 cycles at 0.1 C. The *in situ* study of the electrochemically driven lithiation and delithiation of SnO_2/C nanocomposites in TEM demonstrated that the apparent volume expansion of SnO_2/C chestnut during lithiation is less than that of fully dense SnO_2, and is highly robust, which contributed to its enhanced cycling stability and remarkable rate capability. Our method of synthesis may be extended to produce other hierarchical oxides as well.

Appendix A. Supplementary material

Supplementary data associated with this article can be found in the online version at http://dx.doi.org/10.1016/j.nanoen.2016.08.060.

References

[1] J.M. Tarascon, M. Armand, Nature 414 (2001) 359–367.
[2] V. Etacheri, R. Marom, R. Elazari, G. Salitra, D. Aurbach, Energy Environ. Sci. 4 (2011) 3243–3262.
[3] J. Liang, X.Y. Yu, H. Zhou, H.B. Wu, S. Ding, X.W. Lou, Angew. Chem. Int. Ed. 53 (2014) 12803–12807.
[4] J.S. Chen, X.W. Lou, Small 9 (2013) 1877–1893.
[5] M.S. Park, G.X. Wang, Y.M. Kang, D. Wexler, S.X. Dou, H.K. Liu, Angew. Chem. Int. Ed. 46 (2007) 750–753.
[6] S. Ding, J.S. Chen, X.W. Lou, Adv. Funct. Mater. 21 (2011) 4120–4125.
[7] J.Y. Huang, L. Zhong, C.M. Wang, J.P. Sullivan, W. Xu, L.Q. Zhang, S.X. Mao, N. S. Hudak, X.H. Liu, A. Subramanian, H. Fan, L. Qi, A. Kushima, J. Li, Science 330 (2010) 1515–1520.
[8] R. Retoux, T. Brousse, D.M. Schleich, J. Electrochem. Soc. 146 (1999) 2472–2476.
[9] M. Ebner, F. Marone, M. Stampanoni, V. Wood, Science 342 (2013) 716–720.
[10] J.Y. Cheong, J.H. Chang, H.K. Seo, J.M. Yuk, J.W. Shin, J.Y. Lee, I.-D. Kim, Nano Energy 25 (2016) 154–160.
[11] K. Ui, S. Kawamura, N. Kumagai, Electrochim. Acta 76 (2012) 383–388.
[12] H.B. Wu, J.S. Chen, X.W. Lou, H.H. Hng, J. Phys. Chem. C 115 (2011) 24605–24610.
[13] Y. Zhu, H. Guo, H. Zhai, C. Cao, ACS Appl. Mater. Interfaces 7 (2015) 2745–2753.
[14] L. Zhang, H.B. Wu, X. Wen Lou, Mater. Horiz. 1 (2014) 133–138.
[15] C. Wang, Y. Zhou, M. Ge, X. Xu, Z. Zhang, J.Z. Jiang, J. Am. Chem. Soc. 132 (2010) 46–47.
[16] J. Liu, Y. Li, X. Huang, R. Ding, Y. Hu, J. Jiang, L. Liao, J. Mater. Chem. 19 (2009) 1859–1864.
[17] P. Wu, N. Du, H. Zhang, J. Yu, Y. Qi, D. Yang, Nanoscale 3 (2011) 746–750.
[18] S. Ding, J.S. Chen, G. Qi, X. Duan, Z. Wang, E.P. Giannelis, L.A. Archer, X.W. Lou, J. Am. Chem. Soc. 133 (2011) 21–23.
[19] Y. Yu, C.H. Chen, Y. Shi, Adv. Mater. 19 (2007) 993–997.
[20] X. Zhou, Y.-X. Yin, L.-J. Wan, Y.-G. Guo, J. Mater. Chem. 22 (2012) 17456–17459.
[21] Y.J. Hong, M.Y. Son, Y.C. Kang, Adv. Mater. 25 (2013) 2279–2283.
[22] S. Ding, X. Wen Lou, Nanoscale 3 (2011) 3586–3588.
[23] X.M. Yin, C.C. Li, M. Zhang, Q.Y. Hao, S. Liu, L.B. Chen, T.H. Wang, J. Phys. Chem. C 114 (2010) 8084–8088.
[24] X.W. Lou, C.M. Li, L.A. Archer, Adv. Mater. 21 (2009) 2536–2539.
[25] P. Wu, N. Du, H. Zhang, C. Zhai, D. Yang, ACS Appl. Mater. Interfaces 3 (2011) 1946–1952.
[26] X.H. Liu, L. Zhong, S. Huang, S.X. Mao, T. Zhu, J.Y. Huang, ACS Nano 6 (2012) 1522–1531.
[27] J.S. Cho, Y.C. Kang, Small 11 (2015) 4673–4681.
[28] Y. Yin, R.M. Rioux, C.K. Erdonmez, S. Hughes, G.A. Somorjai, A.P. Alivisatos, Science 304 (2004) 711–714.
[29] H.J. Fan, U. Gösele, M. Zacharias, Small 3 (2007) 1660–1671.
[30] G. Bonn, O. Bobleter, J. Radioanal. Chem. 79 (1983) 171–177.
[31] D. Klingler, H. Vogel, J. Supercrit. Fluids 55 (2010) 259–270.
[32] I.A. Courtney, J.R. Dahn, J. Electrochem. Soc. 144 (1997) 2045–2052.
[33] Z. Wang, Z. Wang, S. Madhavi, X. Wen Lou, J. Mater. Chem. 22 (2012) 2526–2531.
[34] C. Zhu, S. Zhu, K. Zhang, Z. Hui, H. Pan, Z. Chen, Y. Li, D. Zhang, D.-W. Wang, Sci. Rep. 6 (2016) 25829.
[35] S.-Y. Lee, K.-Y. Park, W.-S. Kim, S. Yoon, S.-H. Hong, K. Kang, M. Kim, Nano Energy 19 (2016) 234–245.
[36] X.H. Liu, J.Y. Huang, Energy Environ. Sci. 4 (2011) 3844–3860.